



OPEN

Resonant plasmonic detection of terahertz radiation in field-effect transistors with the graphene channel and the black-As_xP_{1-x} gate layer

V. Ryzhii^{1✉}, C. Tang¹, T. Otsuji¹, M. Ryzhii², V. Mitin³ & M. S. Shur⁴

We propose the terahertz (THz) detectors based on field-effect transistors (FETs) with the graphene channel (GC) and the black-Arsenic (b-As) black-Phosphorus (b-P), or black-Arsenic-Phosphorus (b-As_xP_{1-x}) gate barrier layer. The operation of the GC-FET detectors is associated with the carrier heating in the GC by the THz electric field resonantly excited by incoming radiation leading to an increase in the rectified current between the channel and the gate over the b-As_xP_{1-x} energy barrier layer (BLs). The specific feature of the GC-FETs under consideration is relatively low energy BLs and the possibility to optimize the device characteristics by choosing the barriers containing a necessary number of the b-As_xP_{1-x} atomic layers and a proper gate voltage. The excitation of the plasma oscillations in the GC-FETs leads to the resonant reinforcement of the carrier heating and the enhancement of the detector responsivity. The room temperature responsivity can exceed the values of 10³ A/W. The speed of the GC-FET detector's response to the modulated THz radiation is determined by the processes of carrier heating. As shown, the modulation frequency can be in the range of several GHz at room temperatures.

The emergence of the black-Phosphorus (b-P), black-Arsenic (b-As), and the compounds of these materials (b-AsP), with the energy gap Δ_{BL} varying from 0.15 to 1.2 eV (see, for example,¹⁻²¹) opens new prospects for the creation of different electronic, optoelectronic, and terahertz (THz) devices. The combination of the GLs with the b-As_xP_{1-x} layers with graphene²²⁻²⁸ can be particularly beneficial for the creation of novel devices, including MIR/FIR/THz interband photodetectors. In this paper, we propose and evaluate the THz detectors akin to the field-effect transistors (FETs) with the graphene channel (GC) and b-As_xP_{1-x} gate barrier layer (BL). The operation of such GC-FETs is associated with the carrier heating in the GC by incoming THz radiation (see, for example,²⁹) leading to an increase of the thermionic GC-gate current. This implies that the GC-FETs could operate as hot carrier bolometric detectors. The main features of the proposed THz detectors are as follows: (a) the b-As_xP_{1-x} BL provides the possibility to choose the desirable BL height (and, hence, optimize the device characteristics) by varying the number of the atomic layers and/or the molar fraction of As³⁻⁶, (b) the GC exhibits a room temperature elevated carrier energy relaxation time³⁰⁻³⁴, which promotes high detector responsivities and detectivities, and (c) the plasmonic (PL) properties of the GC-FET³⁵⁻³⁷ can enable the detector resonance response to the THz radiation at the frequencies close to the GC frequencies.

Device structure

Figure 1a shows the GC-FET detector structure (with the number of atomic layers in the BL $N = 20$) and the related band diagrams for the assumed band alignment. For definiteness, we consider the GC-FET structures with the n-type GC, in which the thermionic current between the GC and the gate is associated with the electrons overcoming the BL barrier in the conduction band. If $\Delta_V \geq \Delta_C$, where Δ_C and Δ_V are the band offsets between

¹Research Institute of Electrical Communication, Tohoku University, Sendai 980-8577, Japan. ²Department of Computer Science and Engineering, University of Aizu, Aizu-Wakamatsu 965-8580, Japan. ³Department of Electrical Engineering, University at Buffalo, SUNY, Buffalo, NY 14260, USA. ⁴Department of Electrical, Computer, and Systems Engineering, Rensselaer Polytechnic Institute, Troy, NY 12180, USA. ✉email: v-ryzhii@riec.tohoku.ac.jp

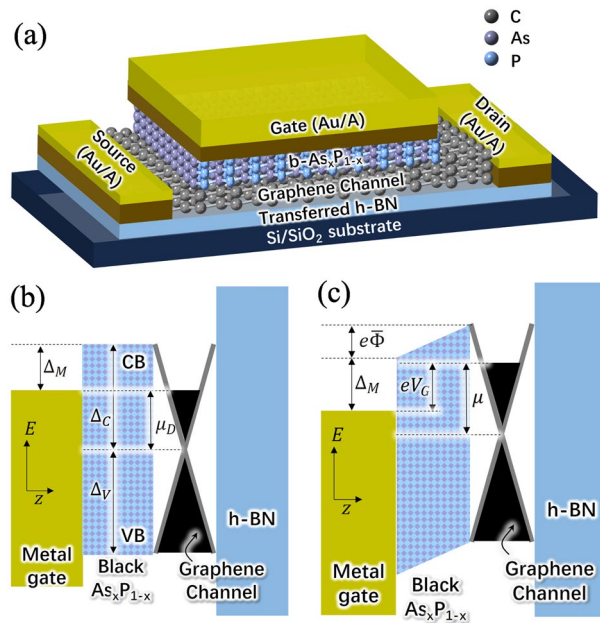


Figure 1. (a) Sketch of the GC-FET detector structure and the band diagrams of the GC-FET with $\Delta_C - \mu_D = \Delta_M$ at (b) $V_G = 0$ (BL flat band condition) and $\bar{j} = 0$, and (c) $V_G > 0$ with $\Delta_C - \mu < \Delta_M$ and $\Delta_V + \mu > \Delta_M$, hence the thermionic electron current density $\bar{j} > 0$ (the hole current is negligible).

the BL conduction and valence band’s edges and the Dirac point in the GC (so that $\Delta_C + \Delta_V$ is the energy gap of the BL), the electron current exceeds the hole current when the electron Fermi energy, μ_D , in the GC is sufficiently large, so that $\Delta_C - \mu_D \lesssim \Delta_M$. Here Δ_M is the difference between the BL and GC work functions and $\mu_D \simeq \hbar v_W \sqrt{\pi \Sigma_D^-}$ is the equilibrium value of the electron Fermi energy counted from the Dirac point at $V_G = 0$, $v_W \simeq 10^8$ cm/s is the characteristic electron velocity in GCs, and \hbar is the reduced Planck constant.

Figures 1b and c show the band diagrams for $\Delta_C - \mu_D = \Delta_M$ at zero gate bias ($V_G = 0$ with the GC donor density Σ_D^- corresponding to the BL flat band) and under the gate bias ($V_G > 0$), respectively. We focus on the GC-FETs with n-doped GC, in which the above equality is met, i.e., assuming that in the absence of the bias gate voltage ($V_G = 0$), the BL bottom of the conduction band and the top of the valence band are flat.

Table 1 lists examples of possible combinations of the b-As_xP_{1-x} barriers and the metal gate materials. The pertinent parameters were taken from¹¹⁻²¹.

The results obtained below can be also used for devices with relatively large Δ_C , considering the hole transport instead of the electron one.

The local voltage drop across the BL $e\Phi = \Delta_C - \Delta_M - \mu + e(V_G + \varphi) = \mu_D - \mu + e(V_G + \varphi)$, where V_G is the applied DC bias gate voltage, $\varphi = \varphi(x, t)$ is the GC potential local value, and μ is the net electron Fermi energy in the GC. At the GC edges, $\varphi(\pm L, t) = \pm \frac{1}{2} \delta V_\omega \exp(-i\omega t)$ or $\varphi(\pm L, t) = \delta V_\omega \exp(-i\omega t)$ for the asymmetric (a) and symmetric (s) THz radiation input, respectively, with δV_ω and ω being the amplitude and the frequency of the THz radiation received by an antenna. The asymmetric THz radiation input corresponds to the design when the antenna leads are connected to the GC-FET side (source and drain) contact pads. In the case of the symmetric input, one of the antenna leads is connected to the gate, whereas the second one to both side contacts.

The variation of the potential difference between the side source and drain contacts (in the case of the symmetrical input) and between the side contacts and the gate leads to the transient electron current along the GC

Sample	x	Metal	Δ_C (meV)	Δ_V (meV)	Δ_M (meV)	μ_D (meV)	Σ_D^- (10^{12}cm^{-2})
Sample 1a	0	Al	225	125	85	140	1.60
Sample 2a	1.0	Al	190	90	50	140	1.60
Sample 1b	0	Ti	225	125	105	120	1.17
Sample 2b	1.0	Ti	190	90	70	120	1.17
Sample 1c	0	In	225	125	135	90	0.66
Sample 2c	0.5	In	230	130	130	100	0.81
Sample 1d	0	Mn	225	125	125	100	0.81
Sample 2d	0.5	Mn	230	130	120	110	0.89

Table 1. Metal gate/b-As_xP_{1-x}/GC barrier layer parameters, $N = 20$, $W = 10 \text{ nm}$ ¹¹⁻²¹.

and the transient variation of the self-consistent electron density, i.e., to the excitation of the plasmonic oscillations. In the case of the asymmetric input, the electron current along the GC exists even at very small signal frequency. As a result the electron heating by the incoming signals takes place at such frequencies as well. In contrast, in the case of the symmetrical input, slow variations of the side contacts potential with respect to the gate potential create a very weak lateral electron current not heating the GC electron system. This leads to marked distinctions of the response in the range of low frequencies (which is demonstrated below).

The BL energy gap Δ_G and the dielectric constant κ_G depend on the transverse electric field Φ/W . Accounting for this, one can set $\Delta_C = \eta\Delta_G[1 - (\Phi/WE_G)^2]$, and $\kappa = \kappa_G/[1 - (\Phi/WE_G)^2]$, where Δ_G and κ are the BL energy gap and the dielectric constant in the absence of the transverse electric field, E_G is the characteristic electric field, W is the BL thickness (see, for example,^{38–41}), and $\eta = \Delta_C/(\Delta_C + \Delta_V) < 1$ the fraction of the atomic layers $N = 20$, $E_G \simeq 0.7 - 0.8 \simeq \text{V/nm}$. This implies that the effect of the transverse electric field on Δ_C , Δ_G , and κ_G markedly reveals at sufficiently high gate voltages when $\Phi \gtrsim 1 \text{ V}$. However, such a voltage range is beyond our present consideration. Considering the GC-FETs with a sufficiently thick b-As_xP_{1-x} BL at moderate gate voltages, we disregard the carrier tunneling across this layer. This implies that the GC-gate current is associated with the sufficiently energetic electrons overcoming the BL, i.e., it is of thermionic origin.

Equations of the model

Thermionic DC and AC. At not-too-small electron densities in GCs, the characteristic time of the electron-electron collisions τ_{ee} is shorter than the pertinent times associated with the optical phonons τ_0 , acoustic phonons τ_{ac} , and impurities τ_i , respectively. This implies that the electron distribution function is close to the Fermi distribution function $f(\varepsilon) = [\exp(\varepsilon - \mu)/T + 1]^{-1}$, characterized by the effective electron temperature T generally different from the lattice (thermostat) temperature T_0 (in the energy units) and the electron Fermi energy μ . Hence, at $\varepsilon > \mu$, $f(\varepsilon) \simeq \exp[(\mu - \varepsilon)/T]$. However, in the energy range $\varepsilon > \Delta_C$, the electron escape over the BL can markedly decrease $f(\varepsilon)$. To account for this effect, in the range in question, one can set $f(\varepsilon) \simeq \xi \exp[(\mu - \varepsilon)/T]$, where $\xi = \tau_{\perp}/(\tau_{ee} + \tau_{\perp})$ with τ_{\perp} being the electron try-to-escape time.

Considering that the height of the potential barrier for the electrons in the GC and in the metal gate are equal to $\Delta_C - \mu$ and $\Delta_M + e(V_G + \varphi)$, respectively, the density of the thermionic electron current can be presented as

$$j \simeq j^{max} \left[\exp\left(\frac{\mu - \Delta_C}{T}\right) - \exp\left(-\frac{\Delta_M + e\Phi}{T_0}\right) \right]. \quad (1)$$

Here $j^{max} = e\Sigma/\tau_{\perp}$ is the characteristic (maximum) GC-gate DC density, Σ is the electron density in the GC induced by the donors and gate voltage, and $e = |e|$ is the electron charge. One can assume that τ_{\perp} is determined by the momentum relaxation time, associated with the quasi-elastic scattering of the high-energy electrons, i.e., with acoustic phonons (in sufficiently perfect GCs). Due to this, it is natural to assume that $\tau_{\perp} > \tau_{ac} \gg \tau_{ee}$. The Fermi energy μ is determined by both the GC doping and the gate voltage.

Equation (1) leads to the following expressions for the thermionic DC density \bar{j} , corresponding to the DC temperature \bar{T} :

$$\bar{j} = j^{max} \left[\exp\left(\frac{\mu - \Delta_C}{\bar{T}}\right) - \exp\left(\frac{\mu - \Delta_C - eV_G}{T_0}\right) \right]. \quad (2)$$

Due to the dependence of μ on V_G , Eq. (2) provides the GC-gate I-V characteristics. Since \bar{T} also depends on V_G (because of the electron heating in the GC by the lateral DC), the latter dependence can somewhat contribute to the GC-FET characteristics as well.

At sufficiently high GC lateral conductivity in the situations under consideration (large Σ and μ), the DC potential and the DC effective temperature nonuniformity along the GC are weak ($\bar{T} \simeq \text{const}$). This implies that we disregard the possible DC crowding. A high electron thermal conductivity additionally suppresses the above nonuniformity.

The AC variation δj_{ω} due to the potential oscillations leading to the electron heating is given by

$$\delta j_{\omega} = j^{max} \frac{\delta T_{\omega}}{\bar{T}} \frac{(\Delta_C - \mu)}{\bar{T}} \exp\left(\frac{\mu - \Delta_C}{\bar{T}}\right) \quad (3)$$

Here we omitted the term containing the factor $(e\delta\varphi_{\omega}/T_0)^2/2$ with $\delta\varphi_{\omega}$ being the GC potential ac component. In this case, the quantity δj_{ω} , given by Eq. (3), does not depend explicitly on the AC variations of the GC potential (only via the effective temperature variation δT_{ω}). This is due to a specific shape of the energy barrier for the electrons in the GC (see Fig. 1c).

Rectified current and effective carrier temperature. The incoming THz radiation results in variations of the potential in the GC. This leads to extra electron heating and the variation of the electron temperature $\delta T = T - \bar{T}$. According to Eq. (3), the variation of the net gate current associated with the effect of the incoming THz radiation averaged over its period (rectified photocurrent) is given by

$$\langle \delta \bar{j}_{\omega} \rangle = j^{max} \mathcal{F}(V_G) \frac{\langle \delta T_{\omega} \rangle}{\bar{T}}. \quad (4)$$

Here $J^{max} = 2LHj^{max}$, and $2L$ and H are the GC length and width,

$$\mathcal{F}(V_G) = \frac{(\Delta_C - \mu)}{\bar{T}} \exp\left(\frac{\mu - \Delta_C}{\bar{T}}\right) = \frac{[\Delta_M - (\mu - \mu_D)]}{\bar{T}} \exp\left[\frac{(\mu - \mu_D) - \Delta_M}{\bar{T}}\right] \quad (5)$$

is the barrier factor, and the symbols $\langle \dots \rangle$ and $\langle \dots \rangle$ denote the averaging over the signal period $2\pi/\omega$ and the length of the GC, respectively, with

$$\langle \delta T_\omega \rangle = \frac{1}{2L} \int_{-L}^L dx \langle \delta T_\omega \rangle. \quad (6)$$

The dependence of the factor $\mathcal{F}(V_G)$ on the gate voltage as associated with the voltage dependence of the electron Fermi energy (see below).

The effective electron temperature T is determined by the balance of the electron energy transfer to the lattice and the energy provided by the electric field along the GL. At room temperature, the emission and absorption of the optical phonons by the electrons in GLs can be considered as a main mechanism of electron energy relaxation. In this case, the power transferring from the electrons in the GC to the optical phonons due to the intraband transitions is^{30–33}.

$$P_0^{intra} = \hbar\omega_0 R_0^{intra}. \quad (7)$$

Here

$$R_0^{intra} = R_0 \frac{\hbar\omega_0 \mu^2}{T_0^3} \left[\left(1 + \frac{1}{\mathcal{N}_0}\right) \exp\left(-\frac{\hbar\omega_0}{T}\right) - 1 \right], \quad (8)$$

$\hbar\omega_0 \sim 200$ meV is the optical phonon energy, $\mathcal{N}_0 = [\exp(\hbar\omega_0/T_0) - 1]^{-1} \simeq \exp(-\hbar\omega_0/T_0)$, R_0 is the characteristic rate of the interband absorption of optical phonons, and T_0 is the lattice temperature. At moderate THz power, the effective electron temperature T is close to the optical phonon temperature T_0 , and Eq. (8) yields for R_0^{intra} .

$$R_0^{intra} \simeq R_0 \frac{\hbar\omega_0 \mu^2}{T_0^3} \left(\frac{1}{T_0} - \frac{1}{T} \right). \quad (9)$$

Equalizing R_0^{intra} given by Eq. (9) and the Joule power associated with the AC in the GC, for the THz range of frequencies (in which one can assume $\omega \gg 1/\tau_\epsilon$), we arrive at the following energy balance equation:

$$\frac{\langle \delta T_\omega \rangle}{\tau_\epsilon} = \frac{\text{Re } \sigma_\omega}{2\Sigma_0 L} \int_{-L}^L dx \left| \frac{d\varphi_\omega}{dx} \right|^2. \quad (10)$$

Here $\text{Re } \sigma_\omega = \sigma_0 v^2 / (v^2 + \omega^2)$ is the real part of the GC Drude conductivity, $\sigma_0 = e^2 \mu / \pi \hbar^2 v$ is its DC value, v is the frequency of the electron collisions on impurities, acoustic phonons, as well as due to the carrier viscosity (see⁴², and the references therein). Accounting for the deviation of the optical phonon temperature T_0 from the lattice temperature T_l , the carrier energy relaxation time τ_ϵ associated with the interaction with optical phonons is estimated as³² $\tau_\epsilon = \tau_0(1 + \xi_0)(T_l/\hbar\omega_0)^2 \exp(\hbar\omega_0/T_l) \simeq \tau_0(1 + \xi_0)(T_0/\hbar\omega_0)^2 \exp(\hbar\omega_0/T_l)$, where τ_0 is the characteristic time of the spontaneous optical phonon intraband emission by the electrons and $\xi_0 = \tau_0^{decay}/\tau_0$, and τ_0^{decay} is the decay time of optical phonons in GCs.

Plasmonic oscillations factor. The description of the spatio-temporal oscillations of the electron density and the self-consistent electric field, i.e., the plasmonic oscillations in the GLs (see, for example^{32–37}) forced by the incoming THz signals can be reduced to a differential equation for the AC potential of the gated GC filled by the electrons (followed from a hydrodynamic electron transport model equations^{43–45} coupled with the Poisson equation), $\delta\varphi_\omega(x)$:

$$\frac{d^2 \delta\varphi_\omega}{dx^2} + \frac{\omega(\omega + i\nu)}{s^2} \delta\varphi_\omega = 0, \quad (11)$$

supplemented by the following boundary conditions:

$$\delta\varphi_\omega|_{x=\pm L} = \pm \frac{\delta V_\omega}{2} \exp(-i\omega t), \quad \delta\varphi_\omega^s|_{x=\pm L} = \delta V_\omega \exp(-i\omega t). \quad (12)$$

Here $s = \sqrt{4e^2 \mu w / \kappa \hbar^2}$ is the plasma-wave velocity in the gated GC.

The above equations yield the following formula for the AC potential along the GC

$$\delta\varphi_\omega^a = \frac{\delta V_\omega \sin(\gamma_\omega x/L)}{2 \sin \gamma_\omega}, \quad \delta\varphi_\omega^s = \delta V_\omega \frac{\cos(\gamma_\omega x/L)}{\cos \gamma_\omega}. \quad (13)$$

Here

$$\gamma_\omega = \pi \frac{\sqrt{\omega(\omega + i\nu)}}{\Omega}, \quad \Omega = \sqrt{\frac{4\pi^2 e^2 \mu W}{\kappa \hbar^2 L^2}} \quad (14)$$

are the normalized wavenumber and the characteristic frequency of the plasmonic oscillations of the electron system in the GC-FET under consideration.

The AC electric field along the GC is equal to

$$\frac{d\varphi_\omega^a}{dx} = \frac{\delta V_\omega}{2} \frac{\gamma_\omega \cos(\gamma_\omega x/L)}{L \sin \gamma_\omega}, \quad \frac{d\varphi_\omega^s}{dx} = -\delta V_\omega \frac{\gamma_\omega \sin(\gamma_\omega x/L)}{L \cos \gamma_\omega} \tag{15}$$

that, accounting for Eq. (12), yields

$$\frac{\langle \delta T_\omega \rangle^{a,s}}{\tau_\epsilon} = \left| \frac{\delta V_\omega}{2} \right|^2 \frac{\sigma_0}{\Sigma L^2} \mathcal{P}_\omega^{a,s}. \tag{16}$$

Here

$$\mathcal{P}_\omega^a = \frac{v^2}{(v^2 + \omega^2)} \int_0^1 d\xi \left| \frac{\gamma_\omega \cos(\gamma_\omega \xi)}{\sin \gamma_\omega} \right|^2, \quad \mathcal{P}_\omega^s = \frac{v^2}{(v^2 + \omega^2)} \int_0^1 d\xi \left| \frac{\gamma_\omega \sin(\gamma_\omega \xi)}{\cos \gamma_\omega} \right|^2 \tag{17}$$

are the plasmonic factors, which can be also presented as

$$\mathcal{P}_\omega^a \simeq \left(\frac{\pi v}{\Omega} \right)^2 \frac{\omega}{\sqrt{(v^2 + \omega^2)}} \frac{P_\omega^a}{|\sin \gamma_\omega|^2}, \quad \mathcal{P}_\omega^s \simeq \left(\frac{\pi v}{\Omega} \right)^2 \frac{\omega}{\sqrt{(v^2 + \omega^2)}} \frac{P_\omega^s}{|\cos \gamma_\omega|^2}, \tag{18}$$

with $P_\omega^a = \int_0^1 d\xi |\cos(\gamma_\omega \xi)|^2$ and $P_\omega^s = \int_0^1 d\xi |\sin(\gamma_\omega \xi)|^2$ being functions of the order of unity oscillating with the frequency. If $\omega \ll \Omega$ (γ_ω tends to zero), Eqs. (17) and (18) yield $\mathcal{P}_\omega^a \simeq 1$ and $\mathcal{P}_\omega^s \simeq 0$.

Combining Eqs. (4), (6), and (16), we obtain

$$\frac{\langle \delta J_\omega \rangle^{a,s}}{J^{max}} = \left| \frac{\delta V_\omega}{2} \right|^2 \frac{\sigma_0 \tau_\epsilon}{\Sigma L^2} \mathcal{F}(V_G) \mathcal{P}_\omega^{a,s}. \tag{19}$$

The detector response depends on the antenna type (see, for example,^{46,47}). Using an antenna specially designed for the THz range could substantially increase the collected power⁴⁷. Here we define the GC-FET detector current responsivity (in the A/W units) and its voltage responsivity (in the V/W units) as

$$\mathcal{R}_\omega = \frac{\langle \delta J_\omega \rangle^{a,s}}{S_\omega}, \quad \mathcal{R}_\omega^V = \frac{\langle \delta J_\omega \rangle^{a,s}}{S_\omega} \rho, \tag{20}$$

respectively. Here S_ω is the THz power collected by an antenna and $\rho = 2L/H\sigma_0$ is the GC DC resistance (for the case of load resistance equal to the GC resistance). This collected power is estimated as $S_\omega = I_\omega A_\omega$, where I_ω is the intensity of the impinging radiation and $A_\omega = \lambda_\omega^2 g/4\pi$ is the antenna aperture⁴⁶, λ_ω is the radiation wavelength, and g is the antenna gain. Considering as an example, the half-wavelength dipole antenna, for which $|\delta V_\omega|^2 \simeq I_\omega (8\pi/c)(\lambda_\omega/\pi)^2$, where c is the speed of light in vacuum, we obtain $|\delta V_\omega|^2 = 32S_\omega/gc$.

Accounting for Eqs. (18) and (19), we obtain

$$\mathcal{R}_\omega = \frac{32 \langle \delta J_\omega \rangle^{a,s}}{gc |\delta V_\omega|^2}, \quad \mathcal{R}_\omega^V = \frac{32 \langle \delta J_\omega \rangle^{a,s}}{gc |\delta V_\omega|^2} \rho. \tag{21}$$

The latter equations yield

$$\mathcal{R}_\omega = \mathcal{R}_0 \mathcal{F}(V_G) \mathcal{P}_\omega^{a,s}, \quad \mathcal{R}_\omega^V = \mathcal{R}_0^V \mathcal{F}(V_G) \mathcal{P}_\omega^{a,s}, \tag{22}$$

where

$$\mathcal{R}_0 = \frac{16 e \sigma_0 \tau_\epsilon H}{g T_c \tau_\perp L}, \quad \mathcal{R}_0^V = \frac{32 e \tau_\epsilon}{g T_c \tau_\perp}. \tag{23}$$

According to Eq. (23), the characteristic voltage responsivity \mathcal{R}_0^V does not explicitly depend on the frequency of electron collisions v .

It is instructive that the responsivity at $V_G = 0$ does not turn to zero because of the factor $\mathcal{F}(0) \neq 0$, so that $\langle \delta J_\omega \rangle > 0$.

Method and results

Equations of the model were analyzed analytically and solved numerically. The resulting GC-FET characteristics—their responsivity found for different device samples are demonstrated in Figs. 2, 3, 4, 5.

Figure 2 shows the normalized responsivity at the fundamental plasmonic resonance $\mathcal{R}_\omega / \mathcal{P}_\omega^a \mathcal{R}_0 |_{\omega=\Omega} = \mathcal{R}_\omega / \mathcal{P}_\omega^s \mathcal{R}_0 |_{\omega=\Omega} = \mathcal{F}(V_G)$ (as a function of the gate voltage V_G) for the devices with different Δ_C , Δ_V , Δ_M , and the GC doping corresponding to the BL flat band at $V_G = 0$ calculated using Eqs. (5) and (20). In this case, the thermionic activation energy $\Delta_C - \mu_D = \Delta_V$. Equations (5) and (20) are supplemented by the following relation for μ accounting for the effect of quantum capacitance^{48–51}:

$$(\mu - \mu_D)(\mu + \mu_D - 2\mu_0) = 2\mu_0 e V_G, \tag{24}$$

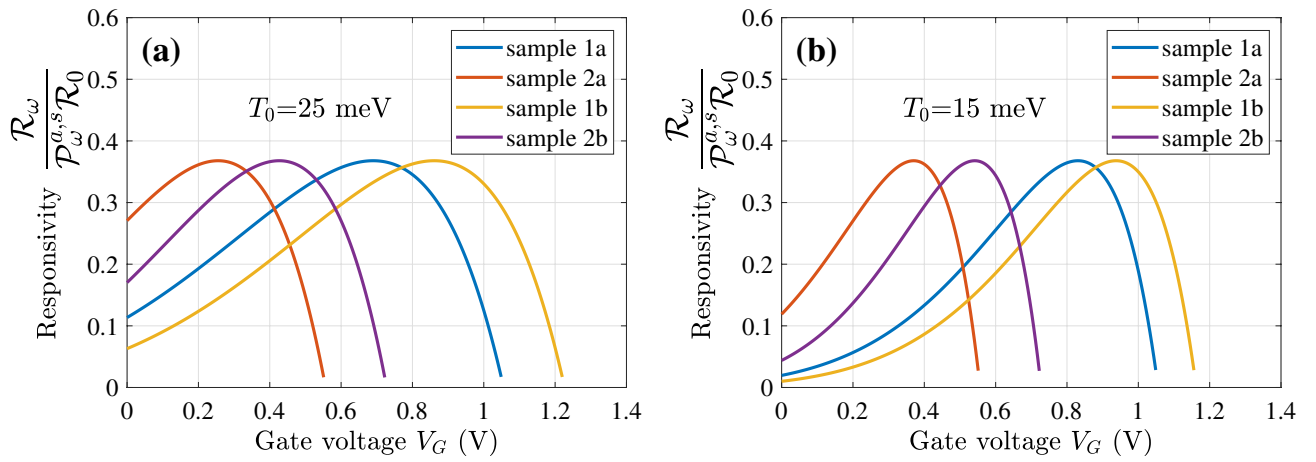


Figure 2. The normalized detector responsivity $\mathcal{R}_\omega / \mathcal{P}_\omega^{a,s} \mathcal{R}_0$ (the same for the asymmetric and symmetric THz radiation input) as a function of the gate voltage V_G for the GC-FETs with different band parameters: (a) at $T_0 = 25$ meV and (b) $T_0 = 15$ meV.

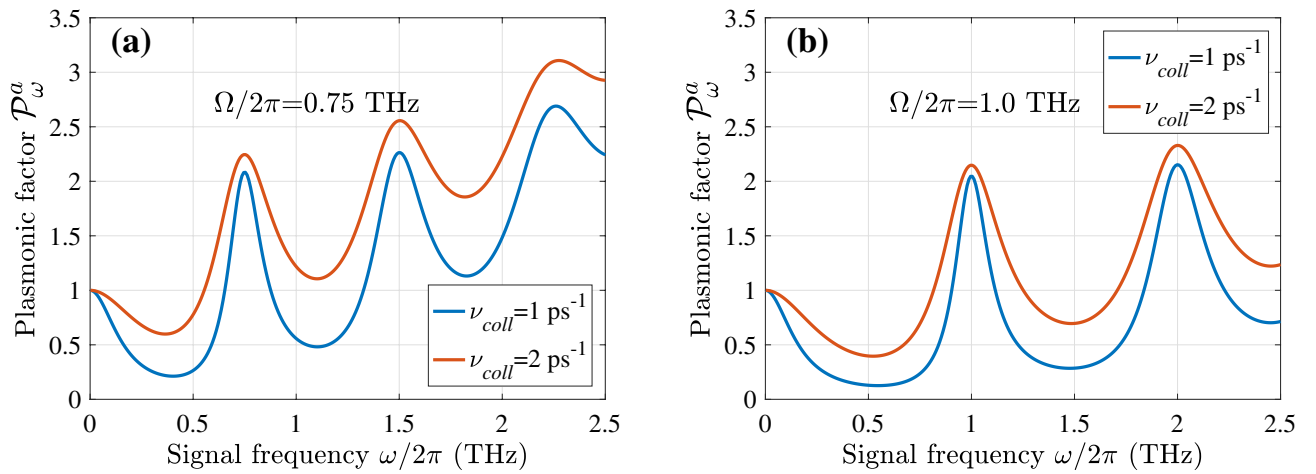


Figure 3. The plasmonic oscillation factor \mathcal{P}_ω^a of the GC-FETs with the asymmetric THz radiation input versus signal frequency $\omega/2\pi$: (a) for $\Omega/2\pi = 0.75$ THz and (b) $\Omega/2\pi = 1.0$ THz ($\nu_{coll} = 1$ ps⁻¹ and 2 ps⁻¹ with $\nu_{visc} = 0.25$ ps⁻¹).

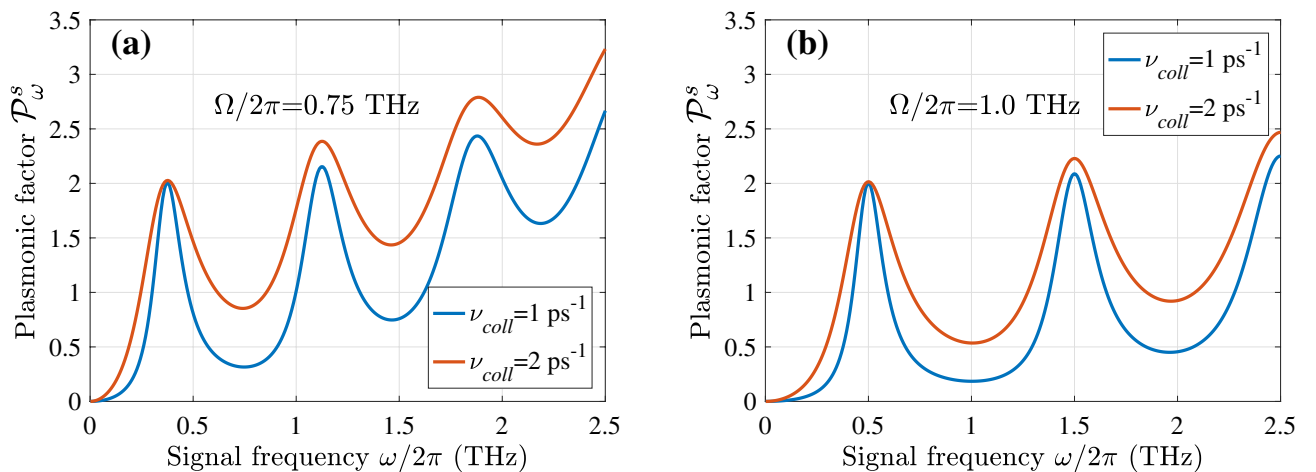


Figure 4. The same as in Fig. 3 but for the plasmonic oscillation factor \mathcal{P}_ω^s of GC-FETs with the symmetric THz radiation input.

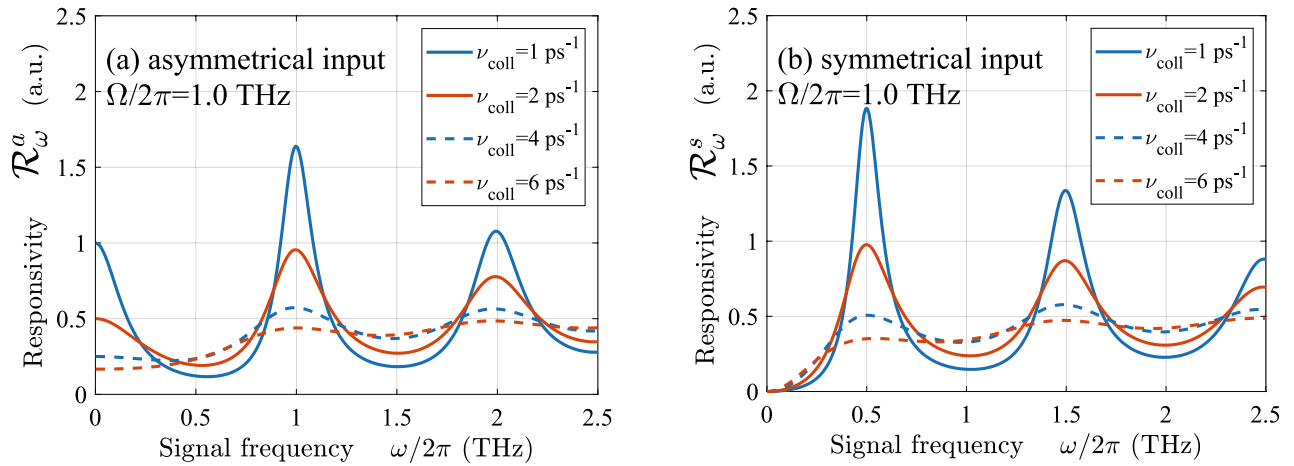


Figure 5. The spectral characteristics of GC-FET detectors current responsivity with (a) asymmetric and (b) symmetric THz radiation input ($\Omega/2\pi = 1.0$ THz) with different collision frequencies ν_{coll} .

where $\mu_0 = (\kappa_G \hbar^2 v_W^2 / 4e^2 W)$. For small (moderate) voltages, Eq. (23) yields

$$\mu \simeq \mu_D + \frac{\mu_0}{(\mu_D + \mu_0)} eV_G. \tag{25}$$

As seen from Fig. 2, the normalized responsivity, which might be rather high at $V_G = 0$, exhibits a maximum at a certain voltage V_G^{max} . The latter is different for different samples depending on the device band parameters. A decrease in the temperature T_0 leads to somewhat sharper responsivity versus gate voltage dependence. This is associated with the specifics of the rectified current-voltage dependence given by Eq. (4). The fact that the maximum of function $\mathcal{F}(V_G)$ height is independent of T_0 is reflected in the dependences shown in Fig. 2.

As follows from Eqs. (18) and (22), the maximal values of \mathcal{R}_ω and \mathcal{R}_ω^V as functions of the signal frequency ω are reached at the plasmonic resonances $\omega = \sqrt{n^2 \Omega^2 - v^2} \simeq n\Omega$ for the asymmetrical input, and $\omega = \sqrt{2n-1} \Omega / 2 \simeq (2n-1)\Omega/2$ for the symmetrical input, where $n = 1, 2, 3, \dots$ is the plasmonic resonance index. At the fundamental resonances, $\mathcal{P}_\omega^a|_{\omega=\Omega} \simeq 2$ and $\mathcal{P}_\omega^s|_{\omega=\Omega/2} \simeq 1$.

Figures 3 and 4 show the frequency dependence of the plasmonic oscillations factors \mathcal{P}_ω^a and \mathcal{P}_ω^s calculated for different values of the plasmonic frequencies Ω and collision frequencies ν . According to Eq. (22), these factors determine (proportional to) the spectral characteristics of the GC-FET detector responsivity. To account for the electron collisions and the effect of their viscosity on the plasmon damping, we set $\nu = \nu_{coll} + \nu_{visc}(\omega/\Omega)^2$, assuming $\nu_{coll} = (1-2) \text{ ps}^{-1}$ and $\nu_{visc} = 0.25 \text{ ps}^{-1}$. In the GC-FETs with $L = (0.5-1.0) \mu\text{m}$, the latter corresponds to the electron viscosity $\hbar \simeq (250-1000) \text{ cm}^2/\text{s}$ that is in line with the observed values⁴².

In particular, Figs. 3 and 4 demonstrate that [in line with Eqs. (17) and (22)] the responsivity exhibits fairly sharp (resonant) maxima at $\omega \simeq n\Omega$ and $\omega \simeq (2n-1)\Omega/2$ when $\nu_{coll} = (1-2) \text{ ps}^{-1}$.

Although the GC-FETs with different methods of the THz radiation input exhibit the resonant response, the pattern of the spectral characteristics shown in these plots are rather distinct, and the resonance frequencies differ. This is associated with the excitation of different plasmonic modes (with different spatial distributions of the ac potential) using asymmetric and symmetric input. As seen, the amplitude of the plasmonic factor maxima increases with increasing resonance index despite the strengthening of the viscosity effect. This is attributed to an increase in the average AC electric field when the number of its semi-periods, i.e., the index n increase.

Figure 5 shows the dependences of the GC-FET detector current responsivity \mathcal{R}_ω corresponding to the plasmonic factors of Figs. 3b and 4b calculated for $\nu_{coll} = 1 \text{ ps}^{-1}$ and $\nu_{coll} = 2 \text{ ps}^{-1}$ (solid lines). These dependences exhibit pronounced plasmonic resonances. Since the responsivity $\mathcal{R}_\omega \propto \sigma_0 \mathcal{P}_\omega \propto \mathcal{P}_\omega / \nu$, the heights of the responsivity peaks for a larger index n and for a larger collisional frequency ν are smaller. It is instructive that the voltage responsivity \mathcal{R}_ω^V for different collisional frequencies exhibits different behavior (at the chosen load resistance, which is assumed to be inversely proportional to σ_0). However, as seen from Fig. 5 (dashed lines), the plasmonic resonances in the cases of much stronger electron scattering ($\nu_{coll} = 4 \text{ ps}^{-1}$ and $\nu_{coll} = 6 \text{ ps}^{-1}$), are substantially smeared.

Using Eq. (14) and setting $\mu = 120-140 \text{ meV}$, $\kappa = 4$, $W = 10 \text{ nm}$, and $L = (1-2) \mu\text{m}$, we obtain the following estimate: $\Omega/2\pi \simeq (0.53-1.14) \text{ THz}$.

Considering that the escape of a hot electron with the energy $\varepsilon \gtrsim \Delta_C$ from the GC over the BL is possible due to its scattering on an acoustic phonon.

We might assume that the electron escape time $\tau_\perp \gg \tau_{ac}$, where τ_{ac} is the momentum relaxation time for the electrons with the energy $\varepsilon \gtrsim \Delta_C$. The quantity τ_{ac} can be estimated as⁵²⁻⁵⁴ $\tau_{ac} \simeq 1 \text{ ps}$. Considering this, for rough estimates at the values Δ_C considered above we set $\tau_\perp \sim 10-20 \text{ ps}$. The electron energy relaxation time due to the interaction with the GC optical phonons is estimated as $\tau_\varepsilon \simeq 32-65 \text{ ps}$ (compare, for example, with^{32,34,55}). The fast decay of optical phonons and the interaction of the electrons in the GC with the interface optical phonons can lead to a decrease in τ_ε to the values about $10-20 \text{ ps}$. Setting $\mu = 140 \text{ meV}$, $\nu = 1 \text{ ps}^{-1}$, $\tau_\perp = 10 \text{ ps}$, $\tau_\varepsilon = 10 \text{ ps}$, $g = 1.64$, $H = 2L$, and $(\Delta_C - \mu)/T_0 = 1$, we arrive at $\mathcal{R}_0 \simeq 4.1 \times 10^2 \text{ A/W}$. This yields

the characteristic voltage responsivity $\mathcal{R}_0^V \simeq 3.7 \times 10^4$ V/W. The latter values are close to the GC-FET current and voltage responsivities, $\mathcal{R}_\omega|_{\omega=\Omega}$ and $\mathcal{R}_\omega^V|_{\omega=\Omega}$, at the plasmonic resonances.

Discussion

In Eq. (10), which governs the electron energy balance in the GC, we disregarded the electron cooling effect, associated with thermionic emission. This effect can be accounted for by replacing the quantity $(\tau_\varepsilon/\tau_\perp)\mathcal{F}(V_G)$ in Eq. (22) by the factor $(\tau_\varepsilon/\tau_\perp)\mathcal{F}(V_G)/[1 + (\tau_\varepsilon/\tau_\perp)\mathcal{F}(V_G)]$. The pertinent distinction is small if $\tau_\varepsilon \lesssim \tau_\perp$.

Using the relation between the GC mobility M and the Fermi energy μ : $M = ev_W^2/v\mu_D$, where the quantity μ_D/v_W^2 is the electron fictitious mass, we find that the values of $v_{coll} = (1 - 2)$ ps⁻¹ and $\mu_D = (120 - 140)$ meV assumed above correspond to $M \simeq (4.3 - 7.1) \times 10^4$ cm²/Vs. For $v_{coll} = (4 - 6)$ ps⁻¹ (see the dashed lines in Fig. 5), one obtains $M \simeq (0.7 - 1.8) \times 10^4$ cm²/Vs, which are realistic GC mobilities at room or somewhat lower temperatures^{53,55}. The electron mobility of the GC on b-P studied several years ago⁵⁶, at $T_0 = (15-25)$ meV ($T_0 \simeq (180 - 300)$ K) reaches the values $M \simeq (8 - 9) \times 10^3$ cm²/Vs. This corresponds to $v_{coll} \simeq (8 - 10)$ ps⁻¹. Further improvements in the GC/b-P interface quality or/and using the GC remote doping (see, for example,^{57,58}), one can reduce v_{coll} increasing the plasmonic resonance sharpness. Another option to decrease v_{coll} is to use the positively biased back gate, which can electrically induce a sufficient electron density in the GC and, hence, a proper value of the electron Fermi energy, eliminating the necessity of GC doping. The plasmonic resonances and, hence, the pronounced resonant response of the GC-FET detectors might be more pronounced for larger plasma frequency Ω , i.e., in the devices with shorter GCs (smaller length $2L$). In particular, if $2L = 0.5$ μ m, the plasma oscillations quality factor is about 8.2 even at $v_{coll} = 10$ ps⁻¹. One needs to note that even at relatively high values of v_{coll} , the overdamped plasmonic oscillations can provide elevated GC-FET detector responsivities despite the resonant peaks vanishing.

Electron thermal conductivity along the GC⁵⁹, which leads to the transfer of a portion of the electron heat to the side contacts can reduce the electron temperature and smooth down the spatial nonuniformities of the electron density. The latter can particularly affect the resonant maxima height with increasing plasmonic mode index n .

Fairly high values of the GC-FET responsivity are due to the long electron energy relaxation time τ_ε inherent for GCs. However, the speed of the photodetectors using the hot electron bolometric mechanism is limited by the inverse electron energy relaxation time τ_ε^{-1} (see, for example,^{34,54}). This implies that the operation of the THz GC-FET detectors under consideration (with the parameters used in the above estimates) might be limited to the modulation frequencies in the GHz range.

The GC-FET detector dark current limited detectivity $D_\omega^* = \mathcal{R}_\omega/\sqrt{2e\bar{j}}$ (see, for example,⁶⁰) depends, in particular, on the dark current density. As follows from Eqs. (2) and (25), the dark current density is

$$\bar{j} \simeq j^{max} \exp\left(-\frac{\Delta_M}{T_0}\right) \exp\left[\frac{\mu_0}{(\mu_D + \mu_0)} \frac{eV_G}{T_0}\right] \left[1 - \exp\left(-\frac{eV_G}{T_0}\right)\right]. \quad (26)$$

For low gate voltages ($eV_G < T_0$), the latter tends to zero as $\bar{j} \propto V_G$. Since the responsivity in the limit of small V_G is a constant (see Fig. 2), this implies that the GC-FET detector detectivity as a function of the gate voltage increases with decreasing V_G as

$$D_\omega^* \propto \frac{1}{\sqrt{V_G}}. \quad (27)$$

This also means that at low values of V_G , the GC-FET noises might be determined by other mechanisms (not by the dark current).

If the electron interactions at the GC/b-AsP interface are relatively strong (leading to high values of v_{coll} and preventing the pronounced plasmonic resonance) is a critical issue, the GC-FET structure can be modified by using the length of the gate and the b-AsP layer markedly smaller than the length of the GC $2L$.

In principle, the GC-FET detectors can be based on the p-type GC, in which $\mu_D < 0$. This might exhibit advantages associated with smaller Δ_V compared to Δ_C (see Table 1). In the detectors with the p-type GC, a proper thermionic activation energy $\Delta_V + \mu_D$ can be achieved at smaller μ_D , i.e., at the lower carrier (hole) densities. However, the adequate BL and metal gate band alignment might be a problem. This problem can be avoided in the GC-FET structures, in which both the GC and the gate are made of p-type graphene layers (double-GC-FETs). Such double-GC-FETs can exhibit markedly different plasmonic properties. This is because of the possible plasmonic response of the carriers in the double-GG (see, for example,⁶¹⁻⁶⁷). The plasmonic response in the double-GC-FETs depends on the contacts. Depending on the geometry of these contacts, the plasmonic factor can be a fairly different function of the signal frequency. The bolometric detectors based on the double-GC-FET structures with the barrier b-As_xP_{1-x} are beyond the scope of our present study and require a separate treatment.

Conclusions

We proposed and evaluated the THz graphene-channel- FET detectors with the black-Arsenic, black-Phosphorus, or black-Arsenic-Phosphorus barrier gate layers. The operation of these detectors is associated with the hot carrier bolometric effect, i.e., with the carrier heating by incoming THz radiation, causing their thermionic emission from the graphene channel into the gate. Such a THz GC-FET detector can exhibit fairly high characteristics. The excitation of plasmonic oscillations in the graphene channel leads to a strong resonant enhancement of the detector responsivity and detectivity.

The realization of the proposed GC-FET bolometric detectors with elevated characteristics is enabled by the effective carrier heating in graphene accompanied by the effective plasmonic oscillation excitation and the possibility of a proper band alignment between the graphene channel and the barrier layer.

Data availability

All data generated or analyzed during this study are included in this published article.

Received: 20 January 2023; Accepted: 12 June 2023

Published online: 14 June 2023

References

1. Keyes, R. W. The electrical properties of black phosphorus. *Phys. Rev.* **92**, 580–584 (1953).
2. Asahina, H. & Morita, A. Band structure and optical properties of black phosphorus. *J. Phys. C: Solid State Phys.* **17**, 1839–1852 (1984).
3. Ling, X., Wang, H., Huang, S., Xia, F. & Dresselhaus, M. S. The renaissance of black phosphorus. *Proc. Natl. Acad. Sci. U.S.A.* **112**, 4523–4530 (2015).
4. Cai, Y., Zhang, G. & Zhang, Y. W. Layer-dependent band alignment and work function of few-layer phosphorene. *Sci. Rep.* **4**, 6677 (2014).
5. Xia, F., Wang, H. & Jia, Y. Rediscovering black phosphorus as an anisotropic layered material for optoelectronics and electronics. *Nat. Commun.* **5**, 4458 (2014).
6. Liu, B. *et al.* Black arsenic-phosphorus: Layered anisotropic infrared semiconductors with highly tunable compositions and properties. *Adv. Mater.* **27**, 4423–4429 (2015).
7. Viti, L. *et al.* Black phosphorus terahertz photodetectors. *Adv. Mater.* **27**, 5567–5572 (2015).
8. Guo, Z. *et al.* From black phosphorus to phosphorene: Basic solvent exfoliation, evolution of Raman scattering, and applications to ultrafast photonics. *Adv. Funct. Mater.* **25**, 6996–7002 (2015).
9. Long, M. *et al.* Room temperature high-detectivity mid-infrared photodetectors based on black arsenic phosphorus. *Sci. Adv.* **3**, e1700589 (2017).
10. Liu, T., Tong, L., Huang, X. & Ye, L. Room-temperature infrared photodetectors with hybrid structure based on two-dimensional materials. *Chin. Phys. B* **28**, 017302 (2019).
11. Hu, T., Xu, B. & Hong, J. Two-dimensional $As_{1-x}P_x$ binary compounds: Highly tunable electronic structure and optical properties. *Curr. Appl. Phys.* **17**, 186–191 (2017).
12. Han, R., Feng, S., Sun, D.-M. & Cheng, H.-M. Properties and photodetector applications of two-dimensional black arsenic phosphorus and black phosphorus. *Sci. China Inf. Sci.* **64**, 1–14 (2021).
13. Xie, M. *et al.* A promising two-dimensional solar cell donor: Black arsenic-phosphorus monolayer with 1.54 eV direct bandgap and mobility exceeding $14,000 \text{ cm}^2 \text{ V}^{-1} \text{ s}^{-1}$. *Nano Energy* **28**, 433–439 (2016).
14. Uda, M., Nakamura, A., Yamamoto, T. & Fujimoto, Y. Work function of polycrystalline Ag, Au and Al. *J. Electron Spectrosc. Relat. Phenom.* **88**, 643–648 (1998).
15. Zhu, Z., Guan, J. & Tomanek, D. Structural transition in layered $As_{1-x}P_x$ compounds: A computational study. *Nano Lett.* **15**, 6042–6046 (2015).
16. Young, E. P. *et al.* Wafer-scale black arsenic-phosphorus thin-film synthesis validated with density functional perturbation theory predictions. *ACS Appl. Nano Mater.* **1**, 4737–4745 (2018).
17. Sun, J. *et al.* The electronic structure, mechanical flexibility and carrier mobility of black arsenic-phosphorus monolayers: A first principles study. *Phys. Chem. Chem. Phys.* **18**, 9779–9787 (2016).
18. Liu, F. *et al.* Potential outstanding physical properties of novel black arsenic phosphorus $As_{0.25}P_{0.75}/As_{0.75}P_{0.25}$ phases: A first-principles investigation. *RSC Adv.* **12**, 3745–3754 (2022).
19. Wu, L. *et al.* All-optical logic devices based on black arsenic-phosphorus with strong nonlinear optical response and high stability. *Opto-Electron. Adv.* **5**, 200046 (2022).
20. Li, L. L. *et al.* Single-layer Janus black arsenic-phosphorus (b-AsP): Optical dichroism, anisotropic vibrational, thermal, and elastic properties. *Phys. Rev. B* **101**, 134102 (2020).
21. Shu, H. & Guo, J. Electronic and optical properties of phosphorene-like arsenic phosphorus: A many-body study. *Mater. Res. Express* **5**, 036302 (2018).
22. Ryzhii, V. *et al.* Electrical modulation of terahertz radiation using graphene-phosphorene heterostructures. *Semicond. Sci. Technol.* **33**, 124010 (2018).
23. Ryzhii, V. *et al.* Real-space-transfer mechanism of negative differential conductivity in gated graphene-phosphorene hybrid structures: Phenomenological heating model. *J. Appl. Phys.* **124**, 114501 (2018).
24. Ryzhii, V. *et al.* Negative terahertz conductivity and amplification of surface plasmons in graphene-black phosphorus injection laser heterostructures. *Phys. Rev. B* **100**, 115436 (2019).
25. Gao, A. *et al.* Robust impact-ionization field-effect transistor based on nanoscale vertical Graphene/Black Phosphorus/Indium Selenide heterostructures. *ACS Nano* **14**, 434–441 (2020).
26. Ryzhii, V. *et al.* Far-infrared photodetectors based on graphene/black-AsP heterostructures. *Opt. Express* **28**, 2480–2498 (2020).
27. Jiang, X.-Q. *et al.* Tunneling devices based on graphene/black phosphorus van der Waals heterostructures. *Mater. Res. Express* **7**, 016310 (2020).
28. Parappurath, A. *et al.* Interlayer charge transfer and photodetection efficiency of graphene-transition-metal-dichalcogenide heterostructures. *Phys. Rev. Appl.* **17**, 064062 (2022).
29. Vicarelli, L. *et al.* Graphene field-effect transistors as room-temperature terahertz detectors. *Nat. Mater.* **11**, 865–871 (2012).
30. Strait, J. H. *et al.* Very slow cooling dynamics of photoexcited carriers in graphene observed by optical-pump terahertz-probe spectroscopy. *Nano Lett.* **11**, 4902–4906 (2011).
31. Ryzhii, V. *et al.* Effect of heating and cooling of photogenerated electron-hole plasma in optically pumped graphene on population inversion. *Jpn. J. Appl. Phys.* **50**, 094001 (2011).
32. Ryzhii, V. *et al.* Graphene terahertz uncooled bolometers. *J. Phys. D: Appl. Phys.* **46**, 315107 (2013).
33. Ryzhii, V. *et al.* Graphene vertical hot-electron terahertz detectors. *J. Appl. Phys.* **116**, 114504 (2014).
34. Tamura, K. *et al.* Fast and sensitive terahertz detection with a current-driven epitaxial-graphene asymmetric dual-grating-gate field-effect transistor structure. *APL Photonics* **7**, 126101 (2022).
35. Ryzhii, V., Satou, A. & Otsuji, T. Plasma waves in two-dimensional electron-hole system in gated graphene heterostructures. *J. Appl. Phys.* **101**, 024509 (2007).
36. Ryzhii, V., Otsuji, T. & Shur, M. Graphene based plasma-wave devices for terahertz applications. *Appl. Phys. Lett.* **116**, 140501 (2020).

37. Ryzhii, V. *et al.* Resonant plasmonic terahertz detection in vertical graphene-base hot-electron transistors. *J. Appl. Phys.* **118**, 204501 (2015).
38. Deng, B. *et al.* Efficient electrical control of thin-film black phosphorus bandgap. *Nat. Commun.* **8**, 14474 (2017).
39. Liu, Y. *et al.* Gate-tunable giant Stark effect in few-layer black phosphorus. *Nano Lett.* **17**, 1970–1977 (2017).
40. Yu, L. *et al.* Electrically tunable optical properties of few-layer black arsenic phosphorus. *Nanotechnology* **29**, 484001 (2018).
41. Kumar, P. *et al.* Thickness and electric-field-dependent polarizability and dielectric constant in phosphorene. *Phys. Rev. B* **93**, 195328 (2016).
42. Zhang, Y. & Shur, M. S. Collision dominated, ballistic, and viscous regimes of terahertz plasmonic detection by graphene. *J. Appl. Phys.* **129**, 053102 (2021).
43. Svintsov, D. *et al.* Hydrodynamic model for electron-hole plasma in graphene. *J. Appl. Phys.* **111**, 083715 (2012).
44. Tomadin, A. & Polini, M. Theory of the plasma-wave photoresponse of a gated graphene sheet. *Phys. Rev. B* **88**, 205426 (2013).
45. Svintsov, D. *et al.* Hydrodynamic electron transport and nonlinear waves in graphene. *Phys. Rev. B* **88**, 245444 (2013).
46. Colin, R. E. *Antenna and Radiowave Propagation* (McGraw-Hill, 1985).
47. He, Y. *et al.* An overview of terahertz antennas. *China Comm.* **17**, 124 (2020).
48. Luryi, S. Quantum capacitance devices. *Appl. Phys. Lett.* **52**, 501–503 (1988).
49. John, D. L., Castro, L. C. & Pulfrey, D. L. Quantum capacitance in nanoscale device modeling. *J. Appl. Phys.* **96**, 5180–5184 (2004).
50. Dröscher, S. *et al.* Quantum capacitance and density of states of graphene. *Appl. Phys. Lett.* **96**, 152104 (2010).
51. Tahir, M. & Schwingenschlögl, U. Beating of magnetic oscillations in a graphene device probed by quantum capacitance. *Appl. Phys. Lett.* **101**, 013114 (2012).
52. Vasko, F. T. Voltage and temperature dependences of conductivity in gated graphene heterostructures. *Phys. Rev. B* **76**, 233404 (2007).
53. Hwang, E. H. & Das Sarma, S. Acoustic phonon scattering limited carrier mobility in two-dimensional extrinsic graphene. *Phys. Rev. B* **77**, 115449 (2008).
54. Ryzhii, V. *et al.* Modulation characteristics of uncooled graphene photodetectors. *J. Appl. Phys.* **129**, 214503 (2021).
55. Yankowitz, M. *et al.* Van der Waals heterostructures combining graphene and hexagonal boron nitride. *Nat. Rev. Phys.* **1**, 112 (2019).
56. Liu, Y. *et al.* Mediated colossal magnetoresistance in graphene/black phosphorus heterostructures. *Nano Lett.* **18**, 3377 (2018).
57. Zhou, T. *et al.* Ultratough graphene-black phosphorus films. *PNAS* **117**, 8727 (2020).
58. Gosling, J. H. *et al.* Universal mobility characteristics of graphene originating from charge scattering by ionised impurities. *Comm. Phys.* **4**, 30 (2021).
59. Kim, T. Y., Park, C.-H. & Marzari, N. The electronic thermal conductivity of graphene. *Nano Lett.* **16**, 2439–2443 (2013).
60. Gong, X. *et al.* High-detectivity polymer photodetectors with spectral response from 300 nm to 1450 nm. *Science* **325**, 1665–1667 (2009).
61. Britnell, L. *et al.* Resonant tunnelling and negative differential conductance in graphene transistors. *Nat. Commun.* **4**, 1794 (2013).
62. Feenstra, R. M., Jena, D. & Gu, G. Single-particle tunneling in doped graphene-insulator-graphene junctions. *J. Appl. Phys.* **111**, 043711 (2012).
63. Ryzhii, V., Otsuji, T., Ryzhii, M. & Shur, M. S. Double graphene-layer plasma resonances terahertz detector. *J. Phys. D: Appl. Phys.* **45**, 302001 (2012).
64. Vasko, F. T. Resonant and nondissipative tunneling in independently contacted graphene structures. *Phys. Rev. B* **87**, 075424 (2013).
65. Ryzhii, V. *et al.* Dynamic effects in double graphene-layer structures with inter-layer resonant-tunneling negative conductivity. *J. Phys. D: Appl. Phys.* **46**, 315107 (2013).
66. Ryzhii, V. *et al.* Terahertz photomixing using plasma resonances in double-graphene layer structures. *J. Appl. Phys.* **113**, 174506 (2013).
67. Zhao, Y. *et al.* Negative differential resistance in boron nitride graphene heterostructures: Physical mechanisms and size scaling analysis. *Sci. Rep.* **5**, 10712 (2015).

Acknowledgements

Financial support is provided by The Japan Society for Promotion of Science (KAKENHI Grants # 20K20349 and # 21H04546), Japan; RIEC Nation-Wide Collaborative Research Project # R04/A10; and by AFOSR (contract number FA9550-19-1-0355).

Author contributions

V.R. conceived the device concept and developed its model, C.T. and M.R. conducted the calculations and presented the results, T.O., V.M. and M.S. analyzed the model, obtained results, and provided financial support. All authors reviewed the manuscript.

Competing interests

The authors declare no competing interests.

Additional information

Correspondence and requests for materials should be addressed to V.R.

Reprints and permissions information is available at www.nature.com/reprints.

Publisher's note Springer Nature remains neutral with regard to jurisdictional claims in published maps and institutional affiliations.



Open Access This article is licensed under a Creative Commons Attribution 4.0 International License, which permits use, sharing, adaptation, distribution and reproduction in any medium or format, as long as you give appropriate credit to the original author(s) and the source, provide a link to the Creative Commons licence, and indicate if changes were made. The images or other third party material in this article are included in the article's Creative Commons licence, unless indicated otherwise in a credit line to the material. If material is not included in the article's Creative Commons licence and your intended use is not permitted by statutory regulation or exceeds the permitted use, you will need to obtain permission directly from the copyright holder. To view a copy of this licence, visit <http://creativecommons.org/licenses/by/4.0/>.

© The Author(s) 2023